

Topologically Nontrivial Magnon Bands in Artificial Square Spin Ices with Dzyaloshinskii-Moriya Interaction

Ezio Iacocca^{1,2,*} and Olle Heinonen^{3,4}

¹*Department of Applied Mathematics, University of Colorado, Boulder, Colorado 80309, USA*

²*Department of Physics, Division for Theoretical Physics, Chalmers University of Technology, 412 96 Gothenburg, Sweden*

³*Materials Science Division, Argonne National Laboratory, Lemont, Illinois 60439, USA*

⁴*Northwestern-Argonne Institute for Science and Engineering, Evanston, Illinois 60208, USA*

(Received 21 December 2016; revised manuscript received 6 July 2017; published 20 September 2017)

Systems that exhibit topologically protected edge states are interesting both from a fundamental point of view as well as for potential applications, the latter because of the absence of backscattering and robustness to perturbations. It is desirable to be able to control and manipulate such edge states. Here, we show that artificial square ices can incorporate both features: an interfacial Dzyaloshinskii-Moriya interaction gives rise to topologically nontrivial magnon bands, and the equilibrium state of the spin ice is reconfigurable with different configurations having different magnon dispersions and topology. The topology is found to develop as odd-symmetry bulk and edge magnon bands approach each other so that constructive band inversion occurs in reciprocal space. Our results show that topologically protected bands are supported in square spin ices.

DOI: 10.1103/PhysRevApplied.8.034015

I. INTRODUCTION

Topological insulators [1–6] are generally materials that are insulating in the bulk but have conducting dissipationless edge states [7]. In two dimensions, topological insulators (TIs) include quantum Hall (QH) states [8,9]. QH edge states are metallic and chiral in that electrons on one physical edge move only in one direction; this prohibits backscattering and makes the states dissipationless. The existence of topologically protected edge states is guaranteed if the band structure of the system has a nontrivial topology. A nontrivial topology is characterized by a nonzero Chern number, which is related to the Berry phase that Bloch states $|u_{n,\mathbf{k}}\rangle$, where \mathbf{k} is a wave vector in the first Brillouin zone and n a band index, acquire when transported around a closed loop in the Brillouin zone; the Chern number is the total flux of the Berry phase in the Brillouin zone. Therefore, in order for there to be a nontrivial topology, the Berry phase accumulated around a closed loop cannot be zero. This may happen but is not assured if time-reversal invariance is broken.

Topologically protected edge states are of great interest for potential applications, for example, in information technology or communication systems. These applications extend beyond electronic systems and includes photonic TIs [10,11] as well as certain magnonic crystals [12,13]. In these latter systems, the band structure of spin excitations, or magnons, exhibit a topological order with nontrivial Chern number and protected edge states determined by the

materials set and structure of the systems. However, systems with potential practical applications should be reconfigurable so that the band structure of excitations can be modified with some external control parameter.

Artificial spin ices (ASIs) [14–16] are systems that allow for such reconfiguration. ASIs are composed of geometrically placed magnetic nanoislands coupled through dipolar interactions. These interactions stabilize the nanoislands' magnetization in configurations such that the magnetization at the lattice vertices satisfy an “ice rule” in low-energy states. ASIs are geometrically frustrated by design; that is, not all interactions at a given vertex can be simultaneously minimized, leading to complex energy surfaces with many local energy minima. Consequently, significant efforts have been devoted to control and manipulate the magnetization state either by thermal or applied field protocols [17] or novel geometries [18–22]. From a dynamic perspective, ASIs compose a superlattice that can be considered a magnonic crystal and, therefore, exhibit a rich band structure [23–29]. Consequently, ASIs compose natural systems to explore reconfigurable magnonics [30], where the properties of the spin-wave band structure can be actively controlled [31–37] to achieve functionality, chiefly for miniaturized microwave electronics [38–42].

A promising geometry for reconfigurable magnonics is square ASIs, where the magnetic nanoislands are placed at the sites of a square lattice. As a superlattice, square ASIs are similar to arrays of dipolarly coupled nanodots [28,43] for which analytical methods calculating band diagrams under a macrospin approximation have been developed [44–46]. However, an initial micromagnetic study by Gliga

*ezio.iacocca@colorado.edu

et al. [31] suggested that frustration in square ASIs modifies magnon modes by the existence of underlying defects known as Dirac strings [16]. These defects originate as the ice rule is locally broken, yet conserving the overall topological charge of the system. More recently, experiments in extended square ASI lattices [34] demonstrated that the magnetization ground state determines the features and eigenfrequencies of the magnon modes. This conclusion was supported by a tight-binding-inspired semianalytical model [33] that captures the dominant dipole-dipole, long-range coupling between the nanoislands and, thus, provides a means to numerically compute the square ASI's band structure, otherwise impractical by more accurate models, e.g., micromagnetic simulations.

Square ASIs, though reconfigurable magnonic crystals, have magnon band structures with trivial topologies. It is of great interest to devise magnonic crystals that have nontrivial topological order *and* are reconfigurable. One way to realize such systems is to introduce interfacial Dzyaloshinskii-Moriya interactions (DMIs) [47,48] to ASIs. The DMI generally manifests as a chiral magnetic interaction in three-dimensional systems with broken inversion symmetry and can give rise to topological edge states in pyrochlores [49] and spin textures in uniaxial thin-film ferromagnets such as skyrmions [50–52]. More conveniently, an interfacial DMI can arise when a trivial magnet is deposited as a thin film on a strong spin-orbit scatterer, such as Ta or Pt. This effect has been used experimentally [51] and numerically [52–54] to nucleate and dynamically drive skyrmions at room temperature. The interfacial DMI naturally has a thickness-dependent strength [55] parametrized by an interfacial energy D in units of J/m². Although most of the research on the DMI has focused on topological structures or nonreciprocal spin-wave dispersion in extended films [55,56], the effect of the DMI for spin waves in magnetic nanoislands has been studied only recently [57]. In the context of magnonic square ASIs, the addition of a chiral interfacial DMI suggests the possibility of topological magnon modes and novel features in their band structure.

The purpose of our work is to demonstrate that square ASIs subject to an interfacial DMI admit topologically nontrivial bands analogous to electronic TIs and topologically trivial bands toggled only by the underlying magnetic configuration. In a magnonic system without DMI, the magnons are elliptical revolutions of the magnetization about its local equilibrium direction, and modes at $(\pm\vec{k}, n)$ are degenerate. The form of the interfacial DMI breaks this degeneracy [57] as it gives rise to an effective magnetic field

$$\vec{H}_{\text{DMI}} = \frac{2D}{M_s} [(\nabla \cdot \vec{m})\hat{z} - \nabla m_z] \quad (1)$$

that couples differently to states at \vec{k} and $-\vec{k}$ and, therefore, gives rise to a coherent Berry phase accumulation. We show that by reconfiguring the equilibrium state of the lattice, the

nontrivial topology can be turned off. Moreover, an external, in-plane magnetic field offers another degree of control to toggle topological bands and their propagation direction.

II. SEMIANALYTICAL MODEL

To compute the band structure of a square ASI, it is necessary to calculate the long-range, dipole-dipole-mediated magnon dispersion as a function of the reciprocal wave vector \vec{k} . For each wave vector, the dispersion relation is obtained from small-amplitude perturbations of the Larmor equation

$$\frac{\partial \vec{m}}{\partial t} = -\gamma\mu_0 \vec{m} \times \vec{H}_{\text{eff}}, \quad (2)$$

where γ is the gyromagnetic ratio, μ_0 is the vacuum permeability, \vec{m} is the magnetization vector normalized to the saturation magnetization M_s , and \vec{H}_{eff} is the effective field that includes diverse physical effects. In order to obtain a meaningful dispersion relation, a minimal model for the effective field must include an external field, exchange coupling, anisotropy, and DMI within a nanomagnet as well as dipolar interactions between nanomagnets. Given the cubic decay of the dipolar interactions, solving Eq. (2) with such an effective field composes a daunting task requiring massive computational resources. While such a study can be performed [58], it is attractive to formulate a minimal model that captures the relevant physics of the system and minimizes the computation time. A time-efficient computational method is especially important for exploring the existence of band inversion, which requires a sufficiently resolved band structure. There are many possibilities to tackle this problem such as utilizing under-resolved micromagnetics to reduce the computational overhead (similar to the atomic structures explored in Refs. [12,13]), extrapolate from simpler systems, e.g., in Ref. [59], or utilize periodic boundary conditions to estimate the band structure, e.g., in Ref. [43]. However, these methods neglect important physical effects such as anisotropy and the long-range interactions across a periodic lattice. Instead, a tight-binding-inspired semianalytical model including the relevant physics for square ASIs was recently shown to yield good agreement with both micromagnetic simulations [33] and experiments [34].

The semianalytical method is based on Eq. (2) and relies on the conserved amplitude of the magnetization vector $|\vec{m}| = 1$ to represent small-amplitude perturbations from a homogeneous state as complex amplitudes a . This representation is achieved by performing a Holstein-Primakoff transformation on the magnetization vector

$$a = \frac{m_\xi + im_\eta}{\sqrt{2M_s(M_s + m_\zeta)}}, \quad (3)$$

where $\vec{m} = (m_\xi, m_\eta, m_\zeta)$ such that m_ζ is parallel to the local equilibrium magnetization direction, and (m_ξ, m_η) represent orthogonal, small perturbations [60]. Substituting Eq. (3) into Eq. (2), a Hamiltonian system of equations is obtained as a function of a and a^* following the procedure outlined in Ref. [60]. The resulting Hamiltonian model can be generalized for $2\mathcal{N}$ interacting complex amplitudes and their complex conjugates \underline{a} and \underline{a}^* so that $\partial_t \underline{a} = i\partial_{\underline{a}^*} \mathcal{H}(\underline{a}, \underline{a}^*)$ and $\partial_t \underline{a}^* = -i\partial_{\underline{a}} \mathcal{H}(\underline{a}, \underline{a}^*)$, where $\mathcal{H}(\underline{a}, \underline{a}^*)$ is a Hamiltonian matrix [33]. These equations can be rewritten as an eigenvalue problem by means of Colpa's grand dynamical matrix [61]

$$\omega \underline{\psi} = \mathcal{H} \underline{\psi} = \begin{pmatrix} \mathcal{H}^{(1,2)} & \mathcal{H}^{(2,2)} \\ \mathcal{H}^{(1,1)} & \mathcal{H}^{(2,1)} \end{pmatrix} \underline{\psi} \quad (4)$$

from which we obtain the eigenvalues ω and eigenvectors $\underline{\psi}$ corresponding to each augmented vector of complex amplitudes $[\underline{a}^T, \underline{a}^\dagger]$. Because of the periodic structure of the ASI, we can label the eigenvectors $\underline{\psi}$ by a wave vector \vec{k} in the first Brillouin zone and a band index n . The Hamiltonian matrix \mathcal{H} is related to the effective field via $\mathcal{H} = -\gamma \delta W / (2M_s)$, where $\delta W = -\int \vec{H}_{\text{eff}}(\vec{M}) \cdot d\vec{M}$ is the energy functional. In Ref. [33], the Hamiltonian matrices for an external in-plane field as well as anisotropy, dipole-dipole, and exchange fields were derived. To minimize finite-size errors from the long-range dipole-dipole Hamiltonian matrix, the lattice is allowed to grow until the relative error is no greater than 10^{-6} . For all \vec{k} , the largest lattice computed has 100×100 unit cells. The exchange interactions within the nanomagnet are also critical to correctly describe edge modes [62] that are manifested in the magnon dispersion [32]. Because we are interested in the low-energy sector of the square ASI dynamics, the magnetic nanoislands are divided in three macrospins coupled by an effective exchange strength, which has been shown to return a faithful representation of the lowest-energy bulk and edge modes [33,34].

Here, we extend the model to include the DMI, which means we have to include the effective interfacial DMI field [52] given by Eq. (1). This field favors a chiral tilt of the perpendicular magnetization component that stabilizes helical order in extended films [63]. Therefore, the model must consider a small-amplitude precession about an arbitrary direction of the unit sphere. The resulting Hamiltonian matrices for the effective interfacial DMI field are

$$\mathcal{H}_{\text{DMI}}^{(1,1)} = D' \begin{pmatrix} V_1 & \mathcal{O} & \mathcal{O} & \mathcal{O} \\ \mathcal{O} & H_1 & \mathcal{O} & \mathcal{O} \\ \mathcal{O} & \mathcal{O} & V_1 & \mathcal{O} \\ \mathcal{O} & \mathcal{O} & \mathcal{O} & H_1 \end{pmatrix}, \quad (5a)$$

$$\mathcal{H}_{\text{DMI}}^{(1,2)} = D' \begin{pmatrix} V_2 & \mathcal{O} & \mathcal{O} & \mathcal{O} \\ \mathcal{O} & H_2 & \mathcal{O} & \mathcal{O} \\ \mathcal{O} & \mathcal{O} & V_2 & \mathcal{O} \\ \mathcal{O} & \mathcal{O} & \mathcal{O} & H_2 \end{pmatrix}, \quad (5b)$$

where V_1, V_2, H_1 , and H_2 are 3×3 complex matrices relating the intrainland magnetization components given in Appendix A, and the \mathcal{O} 's are 3×3 zero matrices. The effective DMI parameter in our discrete, macrospin representation is given by

$$D' = \frac{\gamma D}{2M_s t}, \quad (6)$$

where the inverse dependence on thickness reflects the interfacial nature of this effect. However, we stress that the field Eq. (1) is considered to be homogeneous across the thickness; this is a good approximation for thin nanoislands in which the magnetization at any point is uniform through the thickness.

Because the semianalytical method relies on a second-order perturbation of a well-defined magnetization state, the effect of the DMI can be included only as a deviation from such a state, i.e., low DMI strengths. The initial equilibrium states are determined by energy minimization using Eq. (2) with an added Gilbert damping term, which we calculate from full-scale micromagnetic simulations as we detail below.

III. CHERN NUMBER

The introduction of the DMI in a square ASI breaks time-reversal invariance, which suggests that topological modes may exist. To test for topology, we calculate the Chern number c_n for band n defined as

$$c_n = \frac{1}{2\pi i} \int [\partial_x A_y(\vec{k}) - \partial_y A_x(\vec{k})] d^2 k, \quad (7)$$

where $A_\mu = \langle \underline{\psi}(k), \partial_\mu \underline{\psi}(k) \rangle$ is the Berry connection, $\mu = x, y$, and the eigenmodes $\underline{\psi}$ belong to band n . A nonzero Chern number indicates that the band experiences inversion, which in a finite lattice leads to topological edge modes. We stress that the total Chern number of the band structure obtained by summing c_n over the bands n is conserved to zero. Therefore, any nonzero Chern number must be balanced with an opposite-signed Chern number.

The numerical computation of the Chern number is performed following the method given in Ref. [64]. This method relies on lattice gauge theory to calculate the Chern number in a discretized Brillouin zone, minimizing numerical artifacts that might lead to a noninteger Chern number.

IV. EQUILIBRIUM MAGNETIZATION STATES: MICROMAGNETIC SIMULATIONS

The semianalytical model relies on determining the dispersion of small-amplitude modes about an equilibrium state. To determine these states in square ASIs subject to an interfacial DMI, we perform micromagnetic simulations with both MUMAX3 [65] and our in-house, double-precision micromagnetic code used in, e.g., Refs. [52,66–69]. The square ASI unit cell and geometry are schematically shown in Fig. 1(a), with lattice constant $d = 390$ nm. The nanoislands are considered to be identical stadia, with lateral dimensions $l = 290$ nm and $w = 130$ nm, and variable thickness. These sizes are large enough for the nanoislands to support multiple modes. We consider two materials: permalloy (Py) with $M_s = 790$ A/m and $\text{Co}_{75}\text{Fe}_{25}$ with $M_s = 1200$ kA/m, both with exchange stiffness $A = 13$ pJ/m for simplicity. A heavy-metal layer below the square ASI endows the ferromagnetic nanoislands with an interfacial DMI. Numerically, we solve for a square ASI unit cell and impose periodic boundary conditions to simulate an extended lattice. To correctly account for the nanoislands' rounded edges in the micromagnetic finite-difference scheme, we use a rather small cell size of 0.7 nm in plane and 5 nm along the thickness [70]. Both micromagnetic codes return identical ground states.

Two equilibrium configurations are computed: vortex (type-I) and remanent (type-II) states schematically depicted in Figs. 1(b) and 1(c), respectively. The simulation is initialized by setting a homogeneous magnetization in

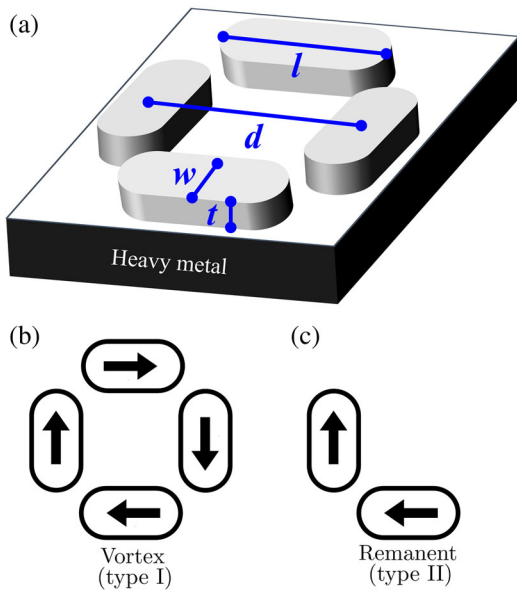


FIG. 1. (a) Schematic of the square ASI unit cell. The composing nanoislands are identical with length l , width w , and thickness t . The lattice constant d is taken as the center-to-center distance between adjacent nanoislands. Interfacial DMI is imparted through a heavy-metal layer. (b) Schematic of a vortex (type-I) unit cell. (c) Schematic of a remanent (type-II) unit cell.

each nanoisland composing either of these states and allowing the simulation to relax using an artificially high Gilbert damping constant $\alpha = 1$. In the remanent state, the equilibrium configurations are S states, and they are insensitive to the DMI strength. In contrast, the vortex state exhibits a richer behavior as a function of D . For $D = 0$, the S states are obtained as shown in Figs. 2(a)–2(c) for the Py nanoislands of thicknesses 10, 15, and 20 nm, where gray scale and arrows represent the \hat{z} and in-plane magnetization component of the topmost layer, respectively. The inclusion of the DMI favors C states for all thicknesses, as shown for $D = 1$ mJ/m² in Figs. 2(d)–2(f). Additionally, the DMI contributes to an out-of-plane tilt of the magnetization at the nanoislands' edges that is odd along the length of the island. However, this tilt is small and does not contribute significantly to the band structure. These simulations confirm that a moderate DMI only slightly perturbs the stable magnetization state in a square ASI, making it possible to study the full band structure by the semianalytical model. We note that labyrinthine, chiral magnetization states are obtained for all thicknesses when $D \geq 3$ mJ/m². For the $\text{Co}_{75}\text{Fe}_{25}$ nanoislands (not shown), a transition between a homogeneous “onion” state and a C state is observed as a function of D .

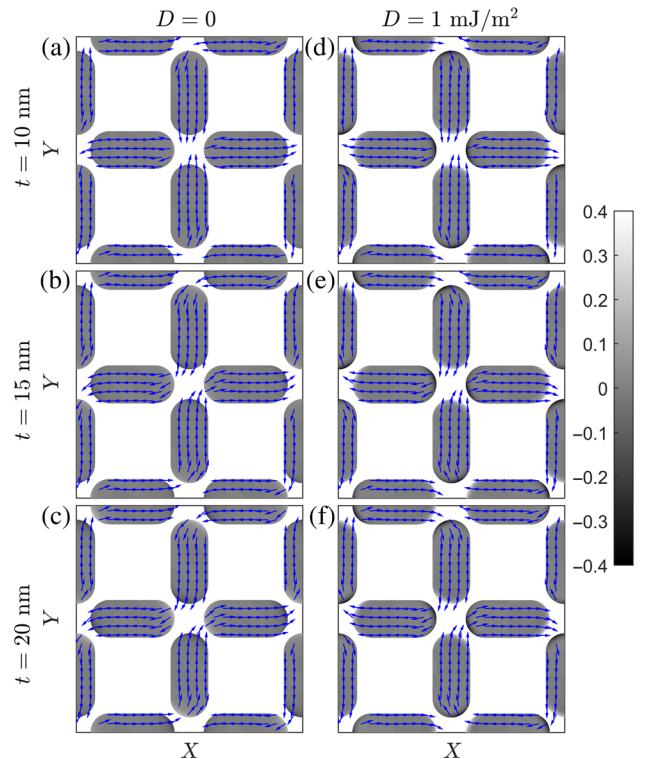


FIG. 2. Micromagnetically computed ground states for a series of Py nanoislands of different thicknesses with (a)–(c) $D = 0$ exhibiting S states and (d)–(f) $D = 1$ mJ/m² exhibiting C states. The gray scale and arrows represent the \hat{z} and in-plane magnetization components, respectively.

The spectrum at the Γ point can be obtained micro-magnetically by analyzing the equilibration after a weak perturbation of the system. We use a spatially homogeneous square field pulse as perturbation, with a duration of 50 ps and a field magnitude of 10 mT applied along the (1,1) direction. The system is then relaxed for 10 ns using a Gilbert damping of $\alpha = 0.01$. This method couples only the uniform field to even modes but allows us to discern the dominant modes in one run. In the remanent state, constant eigenfrequencies are obtained as a function of D , as expected from the negligible impact of the DMI on the equilibrium configuration. These eigenfrequencies are in agreement with those observed in Ref. [33] and are topologically trivial, which we confirm by calculating the Chern numbers of the magnon bands. In the vortex state, the D -dependent eigenfrequencies are shown in Fig. 3 for selected thicknesses of Py [Fig. 3(a)] and $\text{Co}_{75}\text{Fe}_{25}$ nanoislands [Fig. 3(b)]. The empty and filled red circles represent even bulk and edge modes, respectively. We note as a trend that the frequency drops as a function of D , consistent with the lower frequencies in the band diagram

obtained from a C state relative to an S state [33]. It is also important to recognize that whereas we observe a single, fundamental bulk mode, the edge mode frequencies are split, consistent with the spin-wave nonreciprocity induced by the DMI and evidenced by a shift in their dispersion relation [55,57]. However, we note that the frequency splitting is small, on the order of our numerical resolution of 24.5 MHz.

V. BAND STRUCTURE: SEMIANALYTICAL CALCULATIONS

Motivated by the micromagnetic simulations, we now utilize the semianalytical model to solve for the eigenvalues in a square ASI with variable thickness and DMI. As a first step, we validate the semianalytical model by finding the eigenvalues at the Γ point as a function of D in the vortex state. Because of the stadium shape of the nanoislands, we adjust the anisotropy factors estimated to first order by an ellipsoid [71]. This is achieved by setting the equilibrium magnetization estimated from micromagnetic simulations and fitting the bulk and edge mode. For a finite D , we fit the eigenvalues by adjusting the in-plane tilt of the edge magnetization vectors in the semianalytical model and assuming that all nanoislands in the unit cell behave identically. See Appendix B for the fitted parameters. Finally, we extrapolate the in-plane tilt of the edge magnetization vectors by a spline through the fitted points at $D = 0, 0.1, 0.25, 0.5, 0.75,$ and 1 mJ/m^2 . The resulting D -dependent eigenfrequencies at the Γ point are shown in Fig. 3(a) for Py and Fig. 3(b) for $\text{Co}_{75}\text{Fe}_{25}$, where the solid blue and dashed black curves represent the even bulk and edge modes, respectively. Good qualitative agreement between micromagnetic simulations and semianalytical calculations is obtained, suggesting that the semianalytical model captures the relevant physics required to describe the dipole-mediated band structure including the interfacial DMI. We note that the magnetization tilt required to fit the eigenfrequencies is below 25° in all cases, in agreement with the equilibrium states shown in Fig. 2. In the case of 20-nm-thick permalloy nanoislands, the calculated edge mode eigenfrequencies significantly deviate from those obtained micromagnetically. This is a consequence of spatial variations across the thickness of the nanoislands that are not taken into account semianalytically. For $D > 1 \text{ mJ/m}^2$, the DMI strongly perturbs the equilibrium state and dynamics at length scales much smaller than those captured by the three macrospins considered in the semianalytical model ensue.

It is worth noting that the semianalytical model returns a total of 12 bands with three even- and nine odd-symmetry modes. These correspond to the four nanomagnets in the unit cell discretized in three exchange-coupled macrospins. As mentioned before, odd-symmetry modes cannot be excited micromagnetically with a homogeneous field;

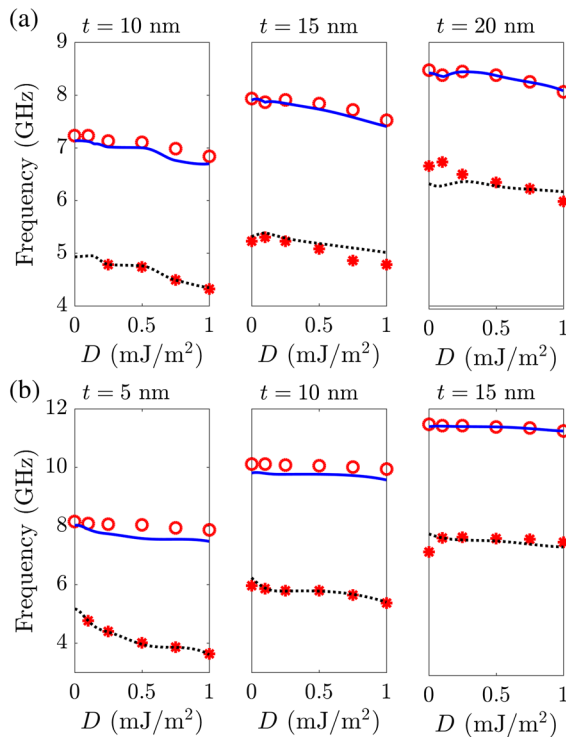


FIG. 3. Even frequencies at the Γ point as a function of D for (a) Py nanoislands of thicknesses $t = 10, 15,$ and 20 nm and (b) $\text{Co}_{75}\text{Fe}_{25}$ nanoislands of thicknesses $t = 5, 10,$ and 15 nm . Good agreement is observed between the even bulk mode obtained semianalytically (solid blue curves) and micromagnetically (empty red circles). The even edge mode obtained semianalytically (dashed black curves) also agrees with those obtained micromagnetically (filled red circles). However, a qualitative deviation of the D dependence for 20-nm-thick Py nanoislands [(a) right panel] is observed.

therefore, the semianalytically obtained odd modes are not shown in Fig. 3.

We now calculate the band structure in the vortex state. For this, we compute the dispersion at $\vec{k} = (k_x, k_y)$ with k_x and k_y discretized in $0.05\pi/d$ composing a surface for each band n in reciprocal space. The bandwise Chern number c_n can be calculated by the method outlined in Sec. III. When $D = 0$, we find $c = 0$ for all thicknesses, as expected from Ref. [33]. However, for $D \neq 0$, we find nonzero Chern numbers for both the bulk and edge odd-symmetry modes. This implies that the DMI breaks the band structure inversion symmetry in reciprocal space.

As an example, we discuss below the first Brillouin zone (FBZ) band diagrams for $D = 0$ (topologically trivial) and $D = 0.75 \text{ mJ/m}^2$ (topologically nontrivial). The symmetry breaking that we discuss above is most clearly seen for the bulk magnon bands by plotting the bands in FBZ^\pm defined as a path through the Γ - X^\pm - M - Γ directions, where the signs represent the relative sign of the k_x and k_y wave-vector components, such that $X^\pm = \pi/(2d)(\hat{k}_x \pm \hat{k}_y)$. For 10-nm-thick Py nanoislands, we show the FBZ for the bulk [Fig. 4(a)] and edge [Fig. 4(b)] odd modes. For the bulk modes and with a DMI of $D = 0.75 \text{ mJ/m}^2$ and FBZ^+ , the bands touch in (small) Dirac cones and exhibit inversion, which, from a topological perspective, indicates constructive Berry phase accumulation and a nonzero Chern number. The band touching is observed in Fig. 4(a) along the Γ - X^+ direction indicated by a red arrow. In contrast, the mirror path in FBZ^- shown in the Fig. 4(a) bottom-right panel does not exhibit a Dirac cone for $D \neq 0$. Additionally, the inequivalence of the two X points in FBZ^+ and FBZ^- is clearly exhibited in the Fig. 4(a) bottom panels. For the edge modes, the Dirac cones occur at a similar point along the Γ - X^+ direction for $D = 0.75 \text{ mJ/m}^2$ shown by the red arrow in Fig. 4(b). Note that these bands do touch along the Γ - M direction both for $D = 0$ and $D \neq 0$, but this does not contribute to the accumulated Berry phase for $D \neq 0$. As expected, the topologically nontrivial bands have oppositely signed Chern numbers maintaining a trivial overall topology so that the sum of the Chern numbers is zero. The same qualitative features are observed in the FBZ for 10-nm-thick $\text{Co}_{75}\text{Fe}_{25}$ nanoislands.

Topological bands appear for DMI strengths as low as $D = 0.1 \text{ mJ/m}^2$ in our simulations. This suggests that topology is a robust feature of the band structure, regardless of the discretization effects of our computation. However, we emphasize that the odd-symmetry bands lie within a range of 200 MHz, representing a challenge for possible measurements at room temperature for these materials because of both intrinsic and extrinsic linewidth broadening that arise from damping and defects (e.g., edge inhomogeneities from patterning), respectively. It may be possible to resolve the bands using, e.g., meander-line resonance absorption [72], provided the measured peaks have very good Lorentzian line

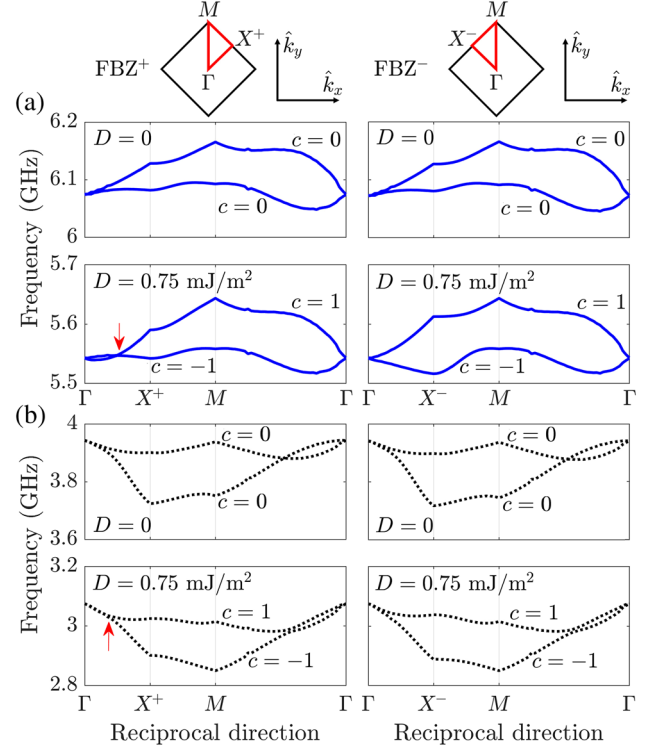


FIG. 4. Band diagram for odd modes in 10-nm-thick Py nanoislands. The FBZ path is depicted at the top of each column. Band diagrams for both $D = 0$ and $D = 0.75 \text{ mJ/m}^2$ are shown. (a) Bulk odd modes exhibit a Dirac cone along the Γ - X direction indicated by a red arrow. The symmetry between the paths FBZ^+ and FBZ^- is broken when $D \neq 0$. (b) Edge modes exhibit band touching in the Γ - M direction, but for the edge mode bands, these do not accumulate Berry phase, and the band touching occurs both for the topologically trivial and nontrivial cases. The Chern number c for each band is specified in each panel.

shape so that careful fitting resolves them. As we discuss in the next section, this issue may be circumvented by applying an external field that both separates the bands and induces Dirac cones along specific directions.

In stark contrast to the qualitative features that we discuss above, the band diagram for the remanent state [see Fig. 1(c)] is topologically trivial as a function of D . This implies that it is possible to toggle between topological and nontopological modes in square ASIs by configuring the underlying magnetization configuration. In other words, ASIs can be utilized as a magnonic crystal with reconfigurable topological bands.

We stress that topologically nontrivial bands arise due to the broken degeneracy of k and $-k$ states in the vortex configuration mediated by an interfacial DMI that allows for a coherent Berry phase accumulation. The accompanying band inversion is a general feature of topologically nontrivial bands and can be further tuned by both material-specific parameters, e.g., saturation magnetization, and geometrical parameters, e.g., nanoislands' shape and lattice constant d and other types of ASIs [18,19,22].

VI. EXTERNAL FIELD DEPENDENCE

An external magnetic field can tune the band frequency both by varying its magnitude $|H|$ and angle θ_H as previously shown for topologically trivial states [33]. Here, we explore the effect of an external, in-plane field on topologically nontrivial bands.

The broken symmetry induced by the DMI suggests that the direction of the applied field can lead to significant changes in the band structure, including loss of topology. We explore the field magnitude dependence of the band structure at $\vec{k} = \pi/d(0.25, 0.25)$, the wave vector at which Dirac cones are observed for bulk modes in both Py and $\text{Co}_{75}\text{Fe}_{25}$ nanoislands of 10 nm in thickness. For Py, the resulting field dependences are shown in Fig. 5(a) when the field is along the (1,0) direction ($\theta_H = 0$, top panel) or the (1,1) direction ($\theta_H = \pi/4$, bottom panel). The bulk bands (blue curves) separate with field and mostly blue-shift. However, the odd-symmetry edge exhibits a more complex behavior with field magnitude and angle. Notably, bands touch for a field of 18 mT along the $\theta_H = \pi/4$ direction indicated by a red arrow. Computing the full band structures at these conditions (not shown) indicates that the bands touch in a Dirac cone and the odd-symmetry edge modes become topologically protected. A similar field dependence is observed for $\text{Co}_{75}\text{Fe}_{25}$ shown in Fig. 5(b). In this case, the field magnitude required to induce a Dirac cone in the odd-symmetry edge modes is 28 mT, consistent with the higher saturation magnetization of $\text{Co}_{75}\text{Fe}_{25}$.

To investigate the onset of Dirac cones at a finite field in more detail, we show in Fig. 6(a) the band structure at $|H| = 18$ mT for Py nanoislands and varying in-plane angle. In the absence of the DMI (top panel), the bands do not touch at any angle. In particular, the band gap between the odd edge modes is approximately 0.5 GHz.

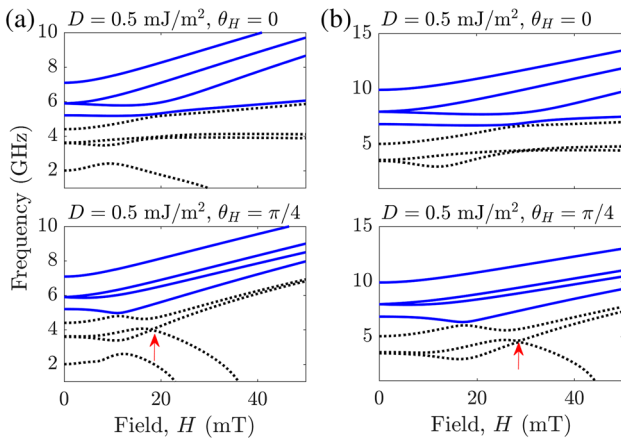


FIG. 5. Field dependence of the band diagram at $\vec{k} = \pi/d(0.25, 0.25)$ for (a) Py and (b) $\text{Co}_{75}\text{Fe}_{25}$. The field is directed along the (1,0) direction in the top panels and along the (1,1) direction in the bottom panels. The red arrows indicate the appearance of a field-dependent Dirac cone at 18 mT for Py and 28 mT for $\text{Co}_{75}\text{Fe}_{25}$.

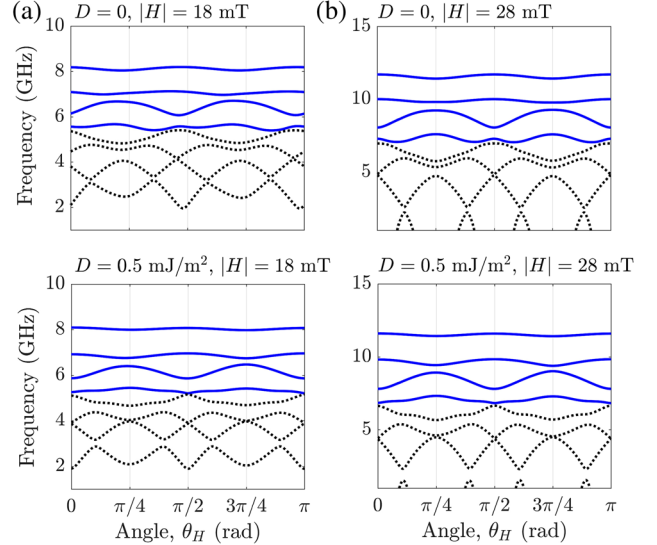


FIG. 6. Angle dependence of the band diagram at $\vec{k} = \pi/d(0.25, 0.25)$ for (a) Py at $|H| = 18$ mT and (b) $\text{Co}_{75}\text{Fe}_{25}$ at $|H| = 28$ mT. Bands do not touch when $D = 0$ (top panels), while Dirac cones are observed in the odd-symmetry edge modes at $\theta_H = \pi/4$ and $3\pi/4$ (bottom panels).

In contrast, for $D = 0.5$ mJ/m², we observe that Dirac cones appear at $\pi/4$ and $3\pi/4$, whereas the bands touching at 0 and π do not accumulate Berry phase. Because the edge modes now span a frequency range of approximately 1 GHz as a function of the angle, this method will allow one to experimentally measure Dirac cones in square ASIs. Similar qualitative results are observed for $\text{Co}_{75}\text{Fe}_{25}$ shown in Fig. 6(b), where the band gap is 1 GHz with $D = 0$ and frequency span of the odd edge modes is 5 GHz.

VII. CONCLUSIONS

In summary, we calculate the spin-wave band structure for square ASIs taking into account an interfacial DMI imparted, e.g., by an adjacent heavy-metal layer. The chiral nature of the DMI influences the eigenmodes supported by the square ASI, leading to band inversion through the development of Dirac cones. Our findings constitute a demonstration that magnon nonreciprocity within a magnetic nanoisland can be manifested at longer wavelengths through dipole coupling, leading to topologically protected edge modes in square ASIs. The magnon bands arise from long-range magnetostatic interactions between modes in individual islands. Only magnon bands that have odd spatial symmetry at the Brillouin zone center ($k = 0$) develop topologically nontrivial modes, consistent with the fact that these bands can more efficiently couple with neighboring spins. It is also observed that topological bands establish a preferred propagation direction that corresponds to the nonreciprocity imparted by the DMI.

The topologically protected magnon bands that we mention above suggest that square ASIs can withstand

both thermal fluctuations and magnon scattering events. This is especially important for magnonic applications where spin waves are required to travel long distances in order to achieve logic and data transfer functionality within an all-magnetic circuitry. Furthermore, these features can be reconfigured, and the nontrivial band topology—and concomitantly topologically protected edge states—can be turned off by changing the underlying magnetization configuration of the square ice, i.e., by different field protocols [34] to relax the nanoislands' magnetization. For instance, one can envision logic circuits based on the preferred propagation direction of topologically protected waves toggled by the reconfiguration of a handful of nanoelements that act as a tunable gate. It is also possible to envision modes propagating at the physical edges of the square ASI lattice exhibiting a much lower decay to magnetic damping based on the nonzero Chern number. However, a finite-sized, discrete lattice can strongly affect the dispersion of surface waves, and a detailed study is required to assess the existence of true (physical) edge modes.

It is noteworthy that topology ensues as the bands approach each other in frequency, making it a challenging measurement due to the spectral broadening arising because of thermal fluctuations at finite temperatures, and spectral mixing. An alternative is to increase the band separation by utilizing an in-plane magnetic field and perform magnitude- and angle-dependent measurements to find evidence of Dirac cones at finite wave vectors. A plausible method to detect the resulting features at finite wave vectors is to use a meander line patterned on top of the square ASI as an antenna with 10-MHz resolution and carefully deconvoluting spectral mixing to discern between the two broad spectral features. By measuring the bands in square ASIs as a function of the spin-orbit scatterer material and the thickness of the magnetic material, it will be possible to experimentally determine the onset of topologically nontrivial bands.

ACKNOWLEDGMENTS

E. I. acknowledges support from the Swedish Research Council, Reg. No. 637-2014-6863. The work by O. H. is funded by the Department of Energy Office of Science, Materials Sciences and Engineering Division. We gratefully acknowledge the computing resources provided on Blues, a high-performance computing cluster operated by the Laboratory Computing Resource Center at Argonne National Laboratory.

APPENDIX A: MATRIX COMPONENTS OF THE DMI HAMILTONIAN

The Hamiltonian matrices are written in terms of the complex amplitudes a , which are related to the normalized

magnetization vector through their spherical components, i.e., the polar and azimuthal angles $\theta = \pi/2$ and φ , respectively (see Refs. [33,60] for details). By performing the cross product $\vec{m}_i \times \vec{m}_j$, where i and j are two neighboring macrospins in a nanoisland, and keeping terms to second order in a , we obtain the 3×3 matrices

$$V_1 = \begin{pmatrix} 0 & R_v^{1,2} & 0 \\ R_v^{2,1} & 0 & R_v^{2,3} \\ 0 & R_v^{3,2} & 0 \end{pmatrix}, \quad (\text{A1a})$$

$$V_2 = \begin{pmatrix} S_v^{1,2} + S_v^{2,1} & C_v^{1,2} & 0 \\ C_v^{2,1} & \sum S_v & C_v^{2,3} \\ 0 & C_v^{3,2} & S_v^{2,3} + S_v^{3,2} \end{pmatrix}, \quad (\text{A1b})$$

$$H_1 = \begin{pmatrix} 0 & R_h^{1,2} & 0 \\ R_h^{2,1} & 0 & R_h^{2,3} \\ 0 & R_h^{3,2} & 0 \end{pmatrix}, \quad (\text{A1c})$$

$$H_2 = \begin{pmatrix} S_h^{1,2} + S_h^{2,1} & C_h^{1,2} & 0 \\ C_h^{2,1} & \sum S_h & C_h^{2,3} \\ 0 & C_h^{3,2} & S_h^{2,3} + S_h^{3,2} \end{pmatrix}, \quad (\text{A1d})$$

where $\sum S_v = S_v^{1,2} + S_v^{2,1} + S_v^{2,3} + S_v^{3,2}$, $\sum S_h = S_h^{1,2} + S_h^{2,1} + S_h^{2,3} + S_h^{3,2}$, and

$$R_v^{i,j} = \sin \theta_i \sin \varphi_i \cos \theta_j - \sin \theta_j \sin \varphi_j \cos \theta_i + i(|\cos \varphi_j| \cos \theta_i - |\cos \varphi_i| \cos \theta_j), \quad (\text{A2a})$$

$$S_v^{i,j} = 2(\cos \theta_j \sin \varphi_j \sin \theta_i - \cos \theta_i \sin \varphi_i \sin \theta_j), \quad (\text{A2b})$$

$$C_v^{i,j} = \sin \theta_j \sin \varphi_j \cos \theta_i - \sin \theta_i \sin \varphi_i \cos \theta_j + i(|\cos \varphi_i| \cos \theta_j + |\cos \varphi_j| \cos \theta_i), \quad (\text{A2c})$$

$$R_h^{i,j} = \sin \theta_i \cos \varphi_i \cos \theta_j - \sin \theta_j \cos \varphi_j \cos \theta_i + i(|\sin \varphi_j| \cos \theta_i - |\sin \varphi_i| \cos \theta_j), \quad (\text{A2d})$$

$$S_h^{i,j} = 2(\cos \theta_j \cos \varphi_j \sin \theta_i - \cos \theta_i \cos \varphi_i \sin \theta_j), \quad (\text{A2e})$$

$$C_h^{i,j} = \sin \theta_j \cos \varphi_j \cos \theta_i - \sin \theta_i \cos \varphi_i \cos \theta_j + i(|\sin \varphi_i| \cos \theta_j + |\sin \varphi_j| \cos \theta_i). \quad (\text{A2f})$$

APPENDIX B: FITTED PARAMETERS FOR THE SEMIANALYTICAL MODEL

To fit micromagnetically to the semianalytically calculated eigenfrequencies, we perform a two-step fitting for the anisotropy factors and the magnetization tilt angles.

TABLE I. Fitted anisotropy factors used in the semianalytical calculations and the first-order estimates from an ellipsoid.

Thickness	Py	Co ₇₅ Fe ₂₅	Ellipsoid [71]
5 nm		$N = 0.957$	$N = 0.9573$
		$L = 0.007$	$L = 0.0139$
		$M = 0.036$	$M = 0.0287$
10 nm	$N = 0.925$	$N = 0.930$	$N = 0.9146$
	$L = 0.020$	$L = 0.014$	$L = 0.0279$
	$M = 0.065$	$M = 0.056$	$M = 0.0575$
15 nm	$N = 0.890$	$N = 0.860$	$N = 0.8720$
	$L = 0.020$	$L = 0.037$	$L = 0.0418$
	$M = 0.090$	$M = 0.103$	$M = 0.0862$
20 nm	$N = 0.780$		$N = 0.8293$
	$L = 0.058$		$L = 0.0557$
	$M = 0.162$		$M = 0.1150$

 TABLE II. Fitted north (N_p) and south (S_p) tilt angles for Py.

D	10 nm	15 nm	20 nm
0 mJ/m ²	$N_p = -10^\circ$	$N_p = -15^\circ$	$N_p = -15^\circ$
	$S_p = -10^\circ$	$S_p = -15^\circ$	$S_p = -15^\circ$
0.10 mJ/m ²	$N_p = -5^\circ$	$N_p = 0^\circ$	$N_p = -1^\circ$
	$S_p = -10^\circ$	$S_p = -10^\circ$	$S_p = 15^\circ$
0.25 mJ/m ²	$N_p = 12^\circ$	$N_p = 10^\circ$	$N_p = 5^\circ$
	$S_p = -12^\circ$	$S_p = -10^\circ$	$S_p = -15^\circ$
0.50 mJ/m ²	$N_p = 13^\circ$	$N_p = 15^\circ$	$N_p = 10^\circ$
	$S_p = -13^\circ$	$S_p = -15^\circ$	$S_p = -10^\circ$
0.75 mJ/m ²	$N_p = 22^\circ$	$N_p = 20^\circ$	$N_p = 15^\circ$
	$S_p = -22^\circ$	$S_p = -20^\circ$	$S_p = -15^\circ$
1.00 mJ/m ²	$N_p = 25^\circ$	$N_p = 25^\circ$	$N_p = 20^\circ$
	$S_p = -25^\circ$	$S_p = -25^\circ$	$S_p = -20^\circ$

 TABLE III. Fitted north (N_p) and south (S_p) tilt angles for Co₇₅Fe₂₅.

D	5 nm	10 nm	15 nm
0 mJ/m ²	$N_p = 0^\circ$	$N_p = 0^\circ$	$N_p = 0^\circ$
	$S_p = 0^\circ$	$S_p = 0^\circ$	$S_p = 0^\circ$
0.10 mJ/m ²	$N_p = 13^\circ$	$N_p = 10^\circ$	$N_p = 4^\circ$
	$S_p = -13^\circ$	$S_p = -8^\circ$	$S_p = -4^\circ$
0.25 mJ/m ²	$N_p = 15^\circ$	$N_p = 10^\circ$	$N_p = 6^\circ$
	$S_p = -15^\circ$	$S_p = -10^\circ$	$S_p = -6^\circ$
0.50 mJ/m ²	$N_p = 20^\circ$	$N_p = 10^\circ$	$N_p = 7^\circ$
	$S_p = -20^\circ$	$S_p = -10^\circ$	$S_p = -7^\circ$
0.75 mJ/m ²	$N_p = 23^\circ$	$N_p = 10^\circ$	$N_p = 10^\circ$
	$S_p = -23^\circ$	$S_p = -12^\circ$	$S_p = -10^\circ$
1.00 mJ/m ²	$N_p = 25^\circ$	$N_p = 17^\circ$	$N_p = 13^\circ$
	$S_p = -25^\circ$	$S_p = -17^\circ$	$S_p = -13^\circ$

The fitted anisotropy factors for Py and Co₇₅Fe₂₅ for each thickness are listed in Table I and compared to the anisotropy factors from an ellipsoid [71]. The nomenclature N , L , M is used for the out-of-plane, easy, and hard-axis anisotropy factors, respectively.

The angles are fitted for each nanoisland to obtain quantitative agreement between the micromagnetic and semianalytic even bulk and edge modes. The fitted angles are listed in Table II for Py and Table III for Co₇₅Fe₂₅. To account for both S and C states, the angles are fitted for both the north (N_p) and south (S_p) macrospins relative to the direction of the magnetization in each nanoisland. The fitted angles in all cases are similar to those obtained by averaging the magnetization angles of the micromagnetic ground states. For example, in the case of Py nanoislands of 15 nm, micromagnetic simulations return north and south tilt angles of 13° and -13° at $D = 0.5$ mJ/m² comparable to the fitted north and south tilt angles of 15° and -15° .

- [1] Joel E. Moore and Leon Balents, Topological invariants of time-reversal-invariant band structures, *Phys. Rev. B* **75**, 121306 (2007).
- [2] David Hsieh, Dong Qian, Lewis Wray, YuQi Xia, Yew San Hor, R. J. Cava, and M. Zahid Hasan, A topological Dirac insulator in a quantum spin Hall phase, *Nature (London)* **452**, 970 (2008).
- [3] David Hsieh, Y. Xia, Dong Qian, L. Wray, J. H. Dil, F. Meier, J. Osterwalder, L. Patthey, J. G. Checkelsky, N. P. Ong *et al.*, A tunable topological insulator in the spin helical Dirac transport regime, *Nature (London)* **460**, 1101 (2009).
- [4] Y. Xia, Dong Qian, David Hsieh, L. Wray, A. Pal, Hsin Lin, Arun Bansil, D. H. Y. S. Grauer, Y. S. Hor, R. J. Cava *et al.*, Observation of a large-gap topological-insulator class with a single Dirac cone on the surface, *Nat. Phys.* **5**, 398 (2009).
- [5] David Hsieh, Y. Xia, L. Wray, Dong Qian, A. Pal, J. H. Dil, J. Osterwalder, F. Meier, G. Bihlmayer, C. L. Kane *et al.*, Observation of unconventional quantum spin textures in topological insulators, *Science* **323**, 919 (2009).
- [6] M. Zahid Hasan and Charles L. Kane, Colloquium: Topological insulators, *Rev. Mod. Phys.* **82**, 3045 (2010).
- [7] Pedram Roushan, Jungpil Seo, Colin V. Parker, Y. S. Hor, David Hsieh, Dong Qian, Anthony Richardella, M. Zahid Hasan, R. J. Cava, and Ali Yazdani, Topological surface states protected from backscattering by chiral spin texture, *Nature (London)* **460**, 1106 (2009).
- [8] D. J. Thouless, Mahito Kohmoto, M. P. Nightingale, and M. den Nijs, Quantized Hall Conductance in a Two-Dimensional Periodic Potential, *Phys. Rev. Lett.* **49**, 405 (1982).
- [9] Qian Niu, D. J. Thouless, and Yong-Shi Wu, Quantized Hall conductance as a topological invariant, *Phys. Rev. B* **31**, 3372 (1985).
- [10] Alexander B. Khanikaev, S. Hossein Mousavi, Wang-Kong Tse, Mehdi Kargarian, Allan H. MacDonald, and Gennady Shvets, Photonic topological insulators, *Nat. Mater.* **12**, 233 (2013).
- [11] Mikael C. Rechtsman, Julia M. Zeuner, Yonatan Plotnik, Yaakov Lumer, Daniel Podolsky, Felix Dreisow, Stefan Nolte, Mordechai Segev, and Alexander Szameit, Photonic Floquet topological insulators, *Nature (London)* **496**, 196 (2013).

- [12] Ryuichi Shindou, Ryo Matsumoto, Shuichi Murakami, and Jun-ichiro Ohe, Topological chiral magnonic edge mode in a magnonic crystal, *Phys. Rev. B* **87**, 174427 (2013).
- [13] Ryuichi Shindou, Jun-ichiro Ohe, Ryo Matsumoto, Shuichi Murakami, and Eiji Saitoh, Chiral spin-wave edge modes in dipolar magnetic thin films, *Phys. Rev. B* **87**, 174402 (2013).
- [14] R. F. Wang, C. Nisoli, R. S. Freitas, J. Li, W. McConville, B. J. Cooley, M. S. Lund, N. Samarth, C. Leighton, V. H. Crespi, and P. Schiffer, Artificial spin ice in a geometrical frustrated lattice of nanoscale ferromagnetic islands, *Nature (London)* **439**, 303 (2006).
- [15] Cristiano Nisoli, Roderich Moessner, and Peter Schiffer, Colloquium: Artificial spin ice: Designing and imaging magnetic frustration, *Rev. Mod. Phys.* **85**, 1473 (2013).
- [16] L. J. Heyderman and R. L. Stamps, Artificial ferroic systems: Novel functionality from structure, interactions and dynamics, *J. Phys. Condens. Matter* **25**, 363201 (2013).
- [17] A. Farhan, P. M. Derlet, A. Kleibert, A. Balan, R. V. Chopdekar, M. Wyss, J. Perron, A. Scholl, F. Nolting, and L. J. Heyderman, Direct Observation of Thermal Relaxation in Artificial Spin Ice, *Phys. Rev. Lett.* **111**, 057204 (2013).
- [18] Ian Gilbert, Gia-Wei Chern, Sheng Zhang, Liam O'Brien, Bryce Foe, Cristiano Nisoli, and Peter Schiffer, Emergent ice rule and magnetic charge screening from vertex frustration in artificial spin ice, *Nat. Phys.* **10**, 670 (2014).
- [19] Ian Gilbert, Yuyang Lao, Isaac Carrasquillo, Liam O'Brien, Justing D. Watts, Michael Manno, Chris Leighton, Andreas Scholl, Cristiano Nisoli, and Peter Schiffer, Emergent reduced dimensionality by vertex frustration in artificial spin ice, *Nat. Phys.* **12**, 162 (2015).
- [20] Yong-Lei Wang, Zhi-Li Xiao, Alexey Snezhko, Jing Xu, Leonidas E. Ocoloa, Ralu Divan, John E. Pearson, George W. Crabtree, and Wai-Kwong Kwok, Rewritable artificial magnetic charge ice, *Science* **352**, 962 (2016).
- [21] F. Ma, C. Reichhardt, Weiliang Gan, C. J. Olson Reichhardt, and W. S. Lew, Emergent geometric frustration of artificial magnetic Skyrmion crystals, *Phys. Rev. B* **94**, 144405 (2016).
- [22] Yann Perrin, Benjamin Canals, and Nicolas Rougemaille, Extensive degeneracy, Coulomb phase and magnetic monopoles in artificial square ice, *Nature (London)*, **540**, 410 (2016).
- [23] S. O. Demokritov and A. N. Slavin, *Magnonics: From Fundamentals to Applications* (Springer, New York, 2013).
- [24] S. A. Nikitov, Ph. Tailhades, and C. S. Tsai, Spin waves in periodic magnetic structures-magnonic crystals, *J. Magn. Magn. Mater.* **236**, 320 (2001).
- [25] S. Neusser and D. Grundler, Magnonics: Spin waves on the nanoscale, *Adv. Mater.* **21**, 2927 (2009).
- [26] V. V. Kruglyak, S. O. Demokritov, and D. Grundler, Magnonics, *J. Phys. D* **43**, 264001 (2010).
- [27] B. Lenk, H. Ulrichs, F. Garbs, and M. Münzenberg, The building blocks of magnonics, *Phys. Rep.* **507**, 107 (2011).
- [28] M. Krawczyk and D. Grundler, Review and prospects of magnonic crystals and devices with reprogrammable band structure, *J. Phys. Condens. Matter* **26**, 123202 (2014).
- [29] A. V. Chumak, V. I. Vasyuchka, A. A. Serga, and B. Hillebrands, Magnon spintronics, *Nat. Phys.* **11**, 453 (2015).
- [30] Dirk Grundler, Reconfigurable magnonics heats up, *Nat. Phys.* **11**, 438 (2015).
- [31] Sebastian Gliga, Attila Kákay, Riccardo Hertel, and Olle G. Heinonen, Spectral Analysis of Topological Defects in an Artificial Spin-Ice Lattice, *Phys. Rev. Lett.* **110**, 117205 (2013).
- [32] Sebastian Gliga, Attila Kákay, Laura J. Heyderman, Riccardo Hertel, and Olle G. Heinonen, Broken vertex symmetry and finite zero-point entropy in the artificial square ice ground state, *Phys. Rev. B* **92**, 060413 (2015).
- [33] Ezio Iacocca, Sebastian Gliga, Robert L. Stamps, and Olle Heinonen, Reconfigurable wave band structure of an artificial square ice, *Phys. Rev. B* **93**, 134420 (2016).
- [34] M. B. Jungfleisch, W. Zhang, E. Iacocca, J. Sklenar, J. Ding, W. Jiang, S. Zhang, J. E. Pearson, V. Novosad, J. B. Ketterson, O. Heinonen, and A. Hoffmann, Dynamic response of an artificial square spin ice, *Phys. Rev. B* **93**, 100401 (2016).
- [35] V. S. Bhat, F. Heimbach, I. Stasinopoulos, and D. Grundler, Magnetization dynamics of topological defects and the spin solid in a kagome artificial spin ice, *Phys. Rev. B* **93**, 140401 (2016).
- [36] Xue Zhou, Geng-Li Chua, Navab Singh, and Adekunle O. Adeyeye, Large area artificial spin ice and anti-spin ice $\text{Ni}_{80}\text{Fe}_{20}$ structures: Static and dynamic behavior, *Adv. Funct. Mater.* **26**, 1437 (2016).
- [37] Qi Wang, Andrii V. Chumak, Lichuan Jin, Huaiwu Zhang, Burkard Hillebrands, and Zhiyong Zhong, Voltage-controlled nanoscale reconfigurable magnonic crystal, *Phys. Rev. B* **95**, 134433 (2017).
- [38] Alexander Khitun, Mingqiang Bao, and Kang L. Wang, Magnonic logic circuits, *J. Phys. D* **43**, 264005 (2010).
- [39] A. D. Karenowska, J. F. Gregg, V. S. Tiberkevich, A. N. Slavin, A. V. Chumak, A. A. Serga, and B. Hillebrands, Oscillatory Energy Exchange between Waves Coupled by a Dynamic Artificial Crystal, *Phys. Rev. Lett.* **108**, 015505 (2012).
- [40] Björn Obyr, Philipp Pirro, Thomas Brächer, Andrii V. Chumak, Julia Osten, Florin Ciubotaru, Alexander A. Serga, Jürgen Fassbender, and Burkard Hillebrands, A microstructured ion-implanted magnonic crystal, *Appl. Phys. Lett.* **102**, 202403 (2013).
- [41] S. Klingler, P. Pirro, T. Brächer, B. Leven, B. Hillebrands, and A. V. Chumak, Design of a spin-wave majority gate employing mode selection, *Appl. Phys. Lett.* **105**, 152410 (2014).
- [42] Marc Vogel, Andrii V. Chumak, Erik H. Waller, Thomas Langner, Vitaliy I. Vasyuchka, Burkard Hillebrands, and Georg von Freymann, Optically reconfigurable magnetic materials, *Nat. Phys.* **11**, 487 (2015).
- [43] S. Tacchi, F. Montoncello, M. Madami, G. Gubbiotti, G. Carlotti, L. Giovannini, R. Zivieri, F. Nizzoli, S. Jain, A. O. Adeyeye, and N. Singh, Band Diagram of Spin Waves in a Two-Dimensional Magnonic Crystal, *Phys. Rev. Lett.* **107**, 127204 (2011).
- [44] P. V. Bondarenko, A. Yu. Galkin, B. A. Ivanov, and C. E. Zaspel, Collective modes for an array of magnetic dots with

- perpendicular magnetization, *Phys. Rev. B* **81**, 224415 (2010).
- [45] Roman Verba, Gennadiy Melkov, Vasil Tiberkevich, and Andrei Slavin, Collective spin-wave excitations in a two-dimensional array of coupled magnetic nanodots, *Phys. Rev. B* **85**, 014427 (2012).
- [46] Ivan Lisenkov, Vasyly Tyberkevych, Sergey Nikitov, and Andrei Slavin, Theoretical formalism for collective spin-wave edge excitations in arrays of dipolarly interacting magnetic nanodots, *Phys. Rev. B* **93**, 214441 (2016).
- [47] I. Dzyaloshinskii, A thermodynamic theory of weak ferromagnetism of antiferromagnetics, *J. Phys. Chem. Solids* **4**, 241 (1958).
- [48] Tôru Moriya, Anisotropic superexchange interaction, and weak ferromagnetism, *Phys. Rev.* **120**, 91 (1960).
- [49] Lifa Zhang, Jie Ren, Jian-Sheng Wang, and Baowen Li, Topological magnon insulator in insulating ferromagnet, *Phys. Rev. B* **87**, 144101 (2013).
- [50] U. Rössler, A. Bogdanov, and C. Pfleiderer, Spontaneous Skyrmion ground states in magnetic metals, *Nature (London)* **442**, 797 (2006).
- [51] Wanjun Jiang, Pramey Upadhyaya, Wei Zhang, Guoqiang Yu, M. Benjamin Jungfleisch, Frank Y. Fradin, John E. Pearson, Yaroslav Tserkovnyak, Kang L. Wang, Olle Heinonen, Suzanne G.E. te Velthuis, and Axel Hoffmann, Blowing magnetic Skyrmion bubbles, *Science* **349**, 283 (2015).
- [52] Olle Heinonen, Wanjun Jiang, Hamoud Smailly, Suzanne G.E. te Velthuis, and Axel Hoffmann, Generation of magnetic Skyrmion bubbles by inhomogeneous spin Hall currents, *Phys. Rev. B* **93**, 094407 (2016).
- [53] J. Sampaio, V. Cros, S. Rohart, A. Thiaville, and A. Fert, Nucleation, stability and current-induced motion of isolated magnetic Skyrmions in nanostructures, *Nat. Nanotechnol.* **8**, 839 (2013).
- [54] Y. Zhou, E. Iacocca, A. Awad, R. K. Dumas, H. B. Zhang, H. B. Braun, and J. Åkerman, Dynamically stabilized magnetic Skyrmions, *Nat. Commun.* **6**, 8193 (2015).
- [55] Hans T. Nembach, Justin M. Shaw, Matthias Weller, Emilie Jué, and Thomas J. Silva, Linear relation between Heisenberg exchange and interfacial Dzyaloshinskii-Moriya interaction in metal films, *Nat. Phys.* **11**, 825 (2015).
- [56] Felipe Garcia-Sanchez, Pablo Borys, Arne Vansteenkiste, Joo-Von Kim, and Robert L. Stamps, Nonreciprocal spin-wave channeling along textures driven by the Dzyaloshinskii-Moriya interaction, *Phys. Rev. B* **89**, 224408 (2014).
- [57] Benjamin W. Zingsem, Michael Farle, Robert L. Stamps, and Robert E. Camley, The unusual nature of confined modes in a chiral system, [arXiv:1609.03417](https://arxiv.org/abs/1609.03417).
- [58] E. K. Semenova, F. Montoncello, S. Tacchi, G. Dürr, E. Sirotkin, E. Ahmad, M. Madami, G. Gubbiotti, S. Neusser, D. Grundler, F. Y. Ogrin, R. J. Hicken, V. V. Kruglyak, D. V. Berkov, N. L. Gorn, and L. Giovannini, Magnetodynamical response of large-area close-packed arrays of circular dots fabricated by nanosphere lithography, *Phys. Rev. B* **87**, 174432 (2013).
- [59] M. Dvornik, P. V. Bondarenko, B. A. Ivanov, and V. V. Kruglyak, Collective magnonic modes of pairs of closely spaced magnetic nano-elements, *J. Appl. Phys.* **109**, 07B912 (2011).
- [60] A. Slavin and V. Tiberkevich, Nonlinear auto-oscillator theory of microwave generation by spin-polarized current, *IEEE Trans. Magn.* **45**, 1875 (2009).
- [61] J. H. P. Colpa, Diagonalization of the quadratic boson Hamiltonian, *Physica A (Amsterdam)* **93A**, 327 (1978).
- [62] G. Carlotti, G. Gubbiotti, M. Madami, S. Tacchi, F. Hartmann, M. Emmerling, M. Kamp, and L. Worschech, From micro- to nanomagnetic dots: Evolution of the eigenmode spectrum on reducing the lateral size, *J. Phys. D* **47**, 265001 (2014).
- [63] Masaya Uchida, Yoshinori Onose, Yoshio Matsui, and Yoshinori Tokura, Real-space observation of helical spin order, *Science* **311**, 359 (2006).
- [64] Takahiro Fukui, Yasuhiro Hatsugai, and Hiroshi Suzuki, Chern numbers in discretized Brillouin zone: Efficient method of computing (spin) Hall conductances, *J. Phys. Soc. Jpn.* **74**, 1674 (2005).
- [65] Arne Vansteenkiste, Jonathan Leliaert, Mykola Dvornik, Mathias Helsen, Felipe Garcia-Sanchez, and Bartel Van Waeyenberge, The design and verification of MUMAX3, *AIP Adv.* **4**, 107133 (2014).
- [66] O. G. Heinonen, D. K. Schreiber, and A. K. Petford-Long, Micromagnetic modeling of spin-wave dynamics in exchange-biased permalloy disks, *Phys. Rev. B* **76**, 144407 (2007).
- [67] D. K. Schreiber, O. G. Heinonen, and A. K. Petford-Long, Micromagnetic modeling of the magnetization dynamics in a circularly exchange-biased and exchange-coupled ferromagnetic multilayer, *Phys. Rev. B* **80**, 014411 (2009).
- [68] P. K. Muduli, O. G. Heinonen, and Johan Åkerman, Bias dependence of perpendicular spin torque and of free- and fixed-layer eigenmodes in MgO-based nanopillars, *Phys. Rev. B* **83**, 184410 (2011).
- [69] Randy K. Dumas, E. Iacocca, S. Bonetti, S. R. Sani, S. M. Mohseni, A. Eklund, J. Persson, O. Heinonen, and Johan Åkerman, Spin-Wave-Mode Coexistence on the Nanoscale: A Consequence of the Oersted-Field-Induced Asymmetric Energy Landscape, *Phys. Rev. Lett.* **110**, 257202 (2013).
- [70] We perform simulations with different in-plane cell size to show that for cells less than about 1.25 nm in plane, the simulations converge and do not exhibit errors because of the “staircase” approximation of the rounded edges. We also perform simulations with a fixed in-plane cell size while varying the perpendicular dimension and find identical results for 5 nm. The cell size of 0.7 nm is chosen on the basis of numerical performance so that the mesh has a number of cells proportional to a power of 2.
- [71] J. A. Osborn, Demagnetizing factors of the general ellipsoid, *Phys. Rev.* **67**, 351 (1945).
- [72] Ching-Ching Tsai, J. Choi, Sunglae Cho, S. J. Lee, Bimal K. Sarma, C. Thompson, O. Chernyashvskyy, Ivan Nevirkovets, and J. B. Ketterson, Microwave absorption measurements using a broad-band meanderline approach, *Rev. Sci. Instrum.* **80**, 023904 (2009).